Materials Advances

ROYAL SOCIETY OF CHEMISTRY

PAPER

View Article Online
View Journal | View Issue

Cite this: *Mater. Adv.*, 2023, 4, 6259

Fluoranthene-based derivatives for multimodal anti-counterfeiting and detection of nitroaromatics†

Kasthuri Selvaraj,[a] Prasanth Palanisamy,[a] Marimuthu Manikandan,[b] Praveen B. Managutti,[c] Palanivelu Sangeetha,[b] Sharmarke Mohamed,[c] Rajesh Pamanji,[d] Joseph Selvin,[d] Sohrab Nasiri,[ef] Stepan Kment[fg] and Venkatramaiah Nutalapati *[a]

In this study, we developed two novel sky blue fluorescent fluorophores comprising ethyl alcohol (**FOH**) and ethanethiol (**FSH**) units appended to fluoranthene at the periphery. Single Crystal X-Ray Diffraction (SC-XRD) studies reveal that the molecular flexibility of alkyl chains leads to distinct diagonal (**FOH**) and ladder (**FSH**) shaped supramolecular arrangements in the crystal lattices. Detailed photophysical and DFT studies showed that **FOH** and **FSH** demonstrate high sensitivity and selectivity towards the detection of trinitrophenol (TNP). **FSH** exhibits high quenching efficiency (~84%), a rate constant of K_{SV} = 1.1 × 10^4 M^{-1} with a limit of detection of ~97 ppm in THF, and ~76 ppm in river water. Mechanistic investigation through NMR and SC-XRD of the **FSH** adduct with 1,3-dinitrobenzene (DNB) reveal strong π–π interactions (3.518 Å). Furthermore, photoinduced electron transfer occurs from the fluorophores to the nitro analytes and leads to strong intermolecular interactions using the static quenching mechanism. Both fluorophores were employed in advanced surveillance to identify finger marks on a wide range of substrates (glass, cellophane tape, aluminium foil and floor tiles) with different resolutions to provide an unadorned and lucrative method for viewing the latent fingerprints (LFPs) with exceptionally consistent evidence of up to level 3 and without the requirement for post-treatments, leading to promising applications for onsite forensic analysis. Furthermore, **FOH** and **FSH** were evaluated in 72 hpf zebrafish larvae/embryos to demonstrate the non-toxicological behaviour and fluorescence imaging/tracking.

Received 30th June 2023,
Accepted 12th October 2023

DOI: 10.1039/d3ma00343d

rsc.li/materials-advances

1. Introduction

Explosive detection and the identification of latent fingerprints (LFPs) play significant roles in counterterrorism and national security issues.[1,2] Because explosive compounds are widely used, the analysis of explosives is vital in forensics, mine detection and global pollution connected to explosion wastes.[3,4] Short and long-term exposure to nitroaromatic explosive materials poses a major risk to anthropoid health for animals and humans, such as anemia, carcinogenic effects and liver damage. Different nitroaromatic compounds (NACs), such as 2,4,6-trinitrophenol (TNP), 2,4,6-trinitrotoluene (TNT) and 2,4-dinitrotoluene (2,4-DNT), comprise the most standard defense explosives and the key considerations of unexploded minefield globally.[5,6] For instance, TNT is listed as an EPA pollutant at concentrations above 2 μg L^{-1}.[7] LFPs are frequently used in criminal investigations and need to be recognized with the correct techniques to determine their origins in conventional forensic practices. Furthermore, the fluorescent illumination of latent finger-marks provides greater clarity, sensitivities, discrimination and device dependence.[8–10] Considering the

[a] *Department of Chemistry, Faculty of Engineering and Technology, SRM Institute of Science and Technology (SRMIST), Kattankulathur-603203, India. E-mail: nvenkat83@gmail.com, venkatrv1@srmist.edu.in*
[b] *Division of Chemistry, School of Advanced Sciences, Vellore Institute of Technology, Chennai, Tamil Nadu 600127, India*
[c] *Chemical Crystallography Laboratory, Khalifa University of Science and Technology, Abu Dhabi, PO Box 127788, United Arab Emirates*
[d] *Department of Microbiology, Pondicherry University, Puducherry 605014, India*
[e] *Faculty of Mechanical Engineering, Optical Measurement Laboratory, Kaunas University of Technology, Studentu Street 56, L-116, Kaunas, LT 51373, Lithuania*
[f] *CEET, Nanotechnology Centre, VŠB-Technical University of Ostrava, 17. Listopadu 2172/15, Ostrava-Poruba 708 00, Czech Republic*
[g] *Czech Advanced Technology and Research Institute, Regional Centre of Advanced Technologies and Materials Department, Palacký University Olomouc, Šlechtitelů 27, Olomouc 78371, Czech Republic*

† Electronic supplementary information (ESI) available: Synthetic procedures, mechanism, characterization of the compounds (NMR, mass, FT-IR), DSC, single crystal X-ray information, optical band gaps, fluorescence titration experiments, Stern–Volmer plots, LODs, real water analysis and toxicological studies on Zebra fish effects are described. CCDC 2179068, 2178647 and 2231960. For ESI and crystallographic data in CIF or other electronic format see DOI: https://doi.org/10.1039/d3ma00343d

ecosystem and the security of users, organic matter for the fluorescence imaging of LFPs has been widely investigated in recent years.[11] Thus, there is a need to create a sensor that is highly selective, sensitive, portable, economical and to develop innovative fingerprint reagent techniques to improve fingerprint performance for the specific purpose of tracing and identification of NACs. Various methods and analytical techniques, such as metal detection, X-ray diffraction, Surface-Enhanced Raman Spectroscopy (SERS), neutron activation, gas chromatography–mass spectrometry (GC-MS), nuclear quadrupole resonance (NQR), ion mobility spectrometers and cyclic voltammetry, are used to identify trace NACs.[12–15] However, the onsite utility of these techniques is restricted owing to their sophisticated instrument and difficulty in handling real-world operations. An alternative approach, such as fluorescence techniques, has received more attention in recent years because of its high sensitivity, quick response, and portability. In recent years, researchers have developed various fluorescent-based sensors, such as metal–organic frameworks,[16] covalent organic polymers,[17] organic–inorganic hybrid materials[18] and quantum dots,[19] to evaluate NACs detection and LFP visualisation.[20–22] However, most of these molecular materials are insoluble in common solvents, making it difficult to fabricate portable devices for practical applications. As an added complication, it is typical to employ identical luminous materials for the recognition of explosives and the identification of LFPs. Furthermore, by employing Aggregation Induced Emission (AIE) and Aggregation Induced Emission Enhancement (AIEE) phenomena to detect nitro analytes at trace levels, with significant focus was made on the synthesis and refinement of innovative conjugated polymers and simple molecule-based related compounds.[23] Although TNP has a higher explosive capacity than TNT (~106% times), it has been attempted to develop chemosensors that can detect TNP at ultra-low levels. Unfortunately, several of these materials are challenged to detect nitro analytes preferentially. Consequently, the scientific research of π-conjugated fluorophores with better properties, greater sensitivity and selective detection has remained a key goal. In this regard, several fluoranthene-based luminescent molecules have been developed as promising chemosensors for TNP by layer-by-layer assembly of fluoranthene and TNP units. The structural alteration by expanding the conjugation with phenyl rings increased detection limits using the contact mode technique.[24–26] Moreover, the influence of the alkyl chain and aromatic substituents on the photophysical characteristics of fluoranthene for the identification of NACs was demonstrated in our previous studies.[27,28] Based on the available literature, developing novel chemosensors with higher selectivity and sensitivity is highly attributed to the fluorophores containing an electron-rich environment and prolonged conjugation. Furthermore, the functional groups of fluorophores should be reacting/hydrophilic to engage in hydrogen bonding and electrostatic interaction with nitro analytes, and substituents at the periphery are advantageous for preventing aggregation.[29a] In this regard, the functionalization of fluorophores plays an important role in the detection of NACs. Moreover, the direct functionalization of fluorophores containing primary alcohol is extremely difficult owing to the poor leaving group nature of primary alcohol. The primary alcohol is necessary to modify into a good leaving group, such as mesylates,[29b] tosylates,[30] and 2,4-nitrobenzene sulfonates,[31] for effective functionalization or substitution. Direct functionalization on primary alcohol achieved a wide range of chemicals, such as unsaturation in steroids,[32–35] ethers[36] and chlorine,[37,38a] *via* tosylation reactions. Allen and co-workers developed various substituted fluoranthene derivatives.[38b] However, to the best of our knowledge, this is the first report to develop a novel method for the direct conversion of primary alcohols to corresponding thiols on fluoranthene by employing various nitrobenzene sulfonates, such as 4-nitrobenzene sulfonyl chloride and 2,4-dinitrobenzene sulfonyl chloride. The orientation of phenyl and various hydrophilic functionalizations, including ethyl alcohol and ethanethiol on the fluoranthene backbone, account for the unique supramolecular arrangements in the solid state. Extensive investigations on the photophysical characteristics in THF and solid state were performed. By varying the functional groups, the hydrophilic and electrostatic attraction of the fluorophore towards detecting NACs have been investigated. **FSH** is highly sensitive and selective for the detection of TNP, with high quenching efficiency (~84%) with detection limits of ~97 ppm (THF) and ~76 ppm (river water). **FOH** and **FSH** fluorophores are employed to visualise high-resolution LFPs on a range of substrates, such as glass, aluminium foil, tiles, and cellophane tape, to study the variation in the emission behaviour when treated with unique nitro explosive compounds.

2. Materials and methods

Sigma Aldrich and S.D. Fine Chemicals Ltd, India provided all A.R. grade chemicals and reagents, which were used without further refinement. NMR (^{1}H and ^{13}C) spectra were collected using a Bruker spectrometer at 500, 400, and 100 MHz, with tetramethylsilane (TMS) as an internal reference. The ESI-MS of the compounds was determined using an Applied Biosystems Voyager DE-STR with microanalysis on a Thermo Finnigan Flash EA 1112 series instrument and assessed using the electrospray ionization (ESI) method. M/S Bruker Daltonik GmbH used QTOF – HRMS with an ESI injector to obtain the HR-MS, and Shimadzu, Irtracer 100 was employed to collect the FT-IR. Differential Scanning Calorimetry (DSC) was performed using NETZSCH DSC 214 with a nitrogen flow of 40 mL min^{-1}. Agilent Cary 60 UV-Vis spectrometer was employed to measure the absorption spectra of the compounds in solution and thin films. The Edinburgh FLS100 Fluorescence Spectrophotometer was used to obtain the fluorescence emission spectra, and the integrated sphere was used to determine the absolute quantum yields. Thin films were obtained by mixing 1 mg of each luminous substance in 0.1 mL of $CHCl_3$ and drop-casting over a quartz plate. The thin films were dried at ambient temperature for 3 h.[39] Time-correlated single-photon counting (TCSPC) technique was utilized to analyze the fluorescence lifetime using a nanosecond LED source (380 nm). Computational studies were carried out using the Gaussian 09 Program by geometry optimization with a basis set of 6-31g* and the hybrid B3LYP parameter.[40]

2.1 Synthesis

7,9-Diphenyl-8*H*-cyclopenta[*a*]acenaphthylen-8-one, **3** was synthesized according to the procedure reported by our group,[28] and detailed analytical characterization is presented in (Scheme S1, ESI†) and Fig. S1 and S2, ESI.† Different functionalized fluoranthene derivatives, such as 2-(7,10-diphenylfluoranthen-8-yl)ethanol (**FOH**) and 2-(7,10-diphenylfluoranthen-8-yl)ethanethiol (**FSH**), were developed, as illustrated in Scheme 1, and their detailed characterization was described in Fig. S3–S8, ESI.† Fig. S9 (ESI†) demonstrates the mechanistic pathway from FOH to FSH. The 2-(7,10-diphenylfluoranthen-8-yl)ethanethiol with 1,3-dinitrobenzene adduct (FSH.DNB) was developed as shown in Scheme S2 (ESI†) and their analytical characterization is represented in Fig. S10–S12 (ESI†).

2.1.1 Synthesis of 2-(7,10-diphenylfluoranthen-8-yl)ethanol (FOH). FOH was synthesized by condensing 7,9-diphenyl-8*H*-cyclopenta[*a*]acenaphthylen-8-one (**3**) (0.5 g, 1.4 mmol) and 3-butynol (**4**) (0.15 g, 2.8 mmol) using diphenyl ether solvent medium in a sealed tube at 225 °C for 26 h. The reaction mixture was isolated by column chromatography using a 20% ethyl acetate/hexane solvent ratio. A pale orange-yellow solid (73% yield) was obtained. ^{1}H NMR (400 MHz, $CDCl_3$) δ 7.76–7.68 (m, 4H), 7.65–7.54 (m, 6H), 7.50–7.45 (m, 2H), 7.40–7.34 (m, 1H), 7.29 (ddd, J = 9.1, 7.6, 3.7 Hz, 3H), 6.44 (d, J = 7.0 Hz, 1H), 3.79 (t, J = 7.0 Hz, 2H), 2.86 (t, J = 6.9 Hz, 2H). ^{13}C NMR (100 MHz, $CDCl_3$) δ 140.70, 139.27, 138.29, 137.89, 137.41, 136.41, 135.87, 135.55, 134.78, 132.75, 130.36, 129.55, 129.25, 129.01, 128.96, 128.51, 127.66, 127.48, 127.40, 126.42, 126.35, 122.98, 122.61, 77.23, 76.91, 76.60, 63.31, 36.09. HR-MS: 399.1794 $[M + 1]^+$.

2.1.2 Synthesis of 2-(7,10-diphenylfluoranthen-8-yl)ethanethiol (FSH). In a 25 mL round bottom flask, **FOH** (250 mg, 0.628 mmol) was taken and solubilized in 5 mL of CH_2Cl_2 under nitrogen gas. To this solution, 4-nitrobenzenesulfonyl chloride (695 mg, 3.14 mmol, 5 equiv.) and triethylamine (3 mL) in 30 mL of CH_2Cl_2 were added dropwise at 0 °C for 30 min. The reaction mixture was brought to ambient temperature for 2 h under a nitrogen environment. During the progress of the reaction, the colour of the reaction mixture was changed from pale yellow-orange to intense yellow-orange. Further, the temperature of the reaction mixture was brought to 40 °C for 48 h. Afterward, the mixture was cooled to room temperature and washed with 1N HCl and brine solution. The solvents were dried over anhydrous Na_2SO_4, filtered, and evaporated under a vacuum. The residue was purified using column chromatography with 15% ethyl acetate/hexane as the eluent. A yellow solid (36% yield) was obtained. ^{1}H NMR (400 MHz, $CDCl_3$) δ 7.74–7.64 (m, 4H), 7.63–7.49 (m, 6H), 7.44 (d, J = 6.3 Hz, 2H), 7.35 (t, J = 7.6 Hz, 1H), 7.30–7.23 (m, 3H), 6.41 (d, J = 7.1 Hz, 1H), 3.61 (t, J = 7.7 Hz, 2H), 3.02 (t, J = 7.7 Hz, 2H). ^{13}C NMR (100 MHz, CDCl3) δ 140.54, 138.80, 138.23, 137.88, 137.09, 136.23, 135.71, 135.19, 135.12, 132.72, 130.37, 129.49, 129.07, 128.89, 128.48, 127.80, 127.67, 127.45, 127.37, 126.43, 122.97, 122.70, 77.16, 76.84, 76.53, 44.29, 36.10, −0.01. HR-MS: 413.2724 $[M - 1]^+$.

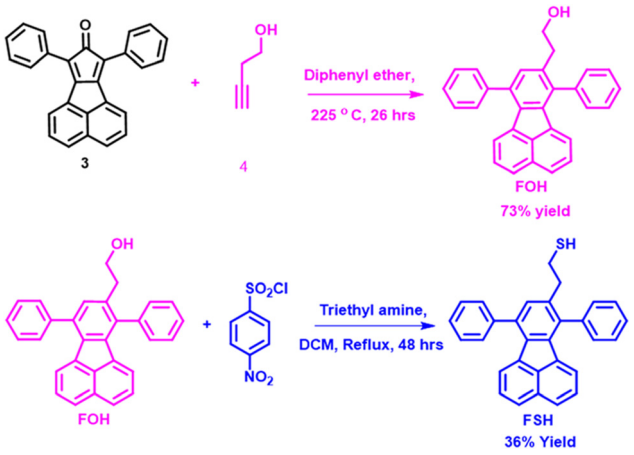

Scheme 1 Synthetic route of **FOH** and **FSH** compounds.

3. Results and discussion

Scheme 1 describes the synthesis of fluoranthene analogues with alkyl chain units, such as alcohol and thiol, at the periphery. As shown in Scheme S1 (ESI†) the Knoevenagel condensation reaction was performed between acenaphthylene-1,2-dione (**1**) and diphenylacetone (**2**), resulting in the formation of 7,9-diphenyl-8*H*-cyclopenta[*a*]acenaphthylen-8-one (**3**) with a 96% yield. Further, the Diels–Alder reaction was carried out between **3** and 3-butynol (**4**) in a diphenyl ether medium at 225 °C to attain 2-(7,10-diphenylfluoranthen-8-yl)ethanol (**FOH**) with a yield of 73%. The HRMS spectrum of **FOH** revealed a molecular ion peak at 399.1794 $[M + 1]^+$, and NMR (^{1}H and ^{13}C) studies confirm in tandem that the expected molecule is the final product. In general, the primary alcohols must be changed into a suitable leaving group, such as mesylates, tosylates and nitrobenzene sulfonates, before they can be functionalized or substituted. Intriguingly, **FSH** was obtained by a single-step reaction using **FOH** in the presence of triethylamine with 4-nitrobenzenesulfonyl chloride. Initially, the 4-nitrobenzenesulfonyl chloride was reacted with basic solvent triethylamine and **FOH** to produce 4-nitrobenzene sulfonate(I), as shown in Fig. S9, ESI.† Further, heating the reaction mixture yields products such as alkenes,[41] chlorides,[42] and pyridinium salts.[43] In this experiment, the 4-nitrobenzene sulfonate(I) was primarily transformed into a chloride, as demonstrated in II (Fig. S9, ESI†). Further, II undergoes 1,2 eliminations, resulting in an alkene product, as illustrated in III. We observed thiol functionalized product IV from alkene III, as depicted in Fig. S9, ESI.† The mechanistic pathway was uncertain for the transition of alkene to thiol functionalization. Furthermore, the HRMS spectrum exhibited a molecular ion peak at 413.2724 $[M - 1]^+$, and NMR (^{1}H and ^{13}C) studies confirm that the predicted **FSH** is the end product. Figs. S13a and b, ESI† show that the ν(O–H) and aromatic ν(C=C) stretched frequencies appear for **FOH** at 3305 and 1601 cm^{-1}, respectively, whereas **FSH** ν(C=C) appears at 1602 cm^{-1}. However, functional

assemblies, such as O–H (702 cm^{-1}) and S–H (700 cm^{-1}) in **FOH** and **FSH**, were evidently distinguished by the fingerprint area. Fig. S14 (ESI†) shows the melting temperature of **FSH** at 152 °C.

FOH exhibits pale-brown crystals grown at ambient temperature using a combination of dichloromethane and methanol (90/10%, v/v) by applying a slow solvent evaporation method. Single crystal X-ray data (293 K) has been solved and refined in the monoclinic crystal system with space group $P2_1/n$, and the unit cell parameters of a = 11.17078(8) Å, b = 20.07704(13) Å, and c = 19.46098(14) Å, with cell volume 4322.83(5) $Å^3$, Z = 8 (CCDC: 2179068) (Fig. 1a and Table S1, ESI†). In the crystal lattice, the molecules are stabilized by strong intra and intermolecular hydrogen bonding, such as O–H···O (1.935 Å) and O···O (3.348 Å) interactions (Fig. 1b). The C–O···H (2.934 Å), aromatic C–H···H (2.486 Å) as well the aromatic $C–H_{aromatic}\cdots\pi$ (2.950 Å) (Fig. S15a, ESI†) interactions are also relevant in contributing to the cohesive intermolecular forces in the crystal. The colourless single crystals of **FSH** were obtained from dimethyl sulfoxide (DMSO) *via* slow solvent evaporation.

As shown in Fig. 1c, **FSH** single crystal was (169.8 K) refined in a monoclinic crystal phase system, space group of $P2_1/c$, and unit cell parameters are a = 28.3784(2) Å, b = 9.76550(10) Å, and c = 23.8510(2) Å, with cell volume 6599.62(10) $Å^3$ with Z = 12 (CCDC: 2178647) (Fig. S15b and Table S1, ESI†). The supramolecular arrangement in the crystal lattice (Fig. 1d) was stabilized by intermolecular hydrogen bonding between C–S···H–C (2.933 Å), S···S (3.802 Å), $C\cdots C_{aromatic}$ (3.449 Å) and $C–S\cdots C_{aromatic}$ (3.517 Å) interactions and C–H···π (2.998 Å). **FSH** is stabilized by a ladder-type topology in the crystal packing in 2D with strong C–H···C (2.971 Å) and $C–H_{aromatic}\cdots\pi$ (2.941 Å) interactions (Fig. S15b and Table S1, ESI†). Fig. 2a illustrates the optical absorption and emission analysis of **FOH** and **FSH** in THF and thin films deposited on quartz glass. In THF (Fig. 2a), both functional ensembles of fluoranthene exhibit two distinct characteristic absorption bands at 291 and 377 nm, respectively, primarily attributed to the π → π* transitions. In thin films, the bands are broadened with an increase in intensity with a bathochromic shift of ∼6 nm ascribed owing to π → π* transitions of weak self-assembled molecular aggregates of alkyl chains at the periphery. The optical band gaps are measured from the low-energy absorption bands, and the data are provided in Table 1. Based on the hetero atom substituents, the optical band gaps were observed to change slightly from a solution to a thin film (Fig. S16a–d, ESI†). The optical energy band gaps for **FOH** and **FSH** are 2.86 and 2.82 eV, respectively.

Both fluorophores emit an intense blue emission at ∼450 ± 3 nm with a Stoke's shift of ∼79 ± 3 nm in THF (Fig. 2b). Compared to **FOH**, the emission spectrum of **FSH** is slightly blue-shifted. Owing to the presence of thiol as a significant

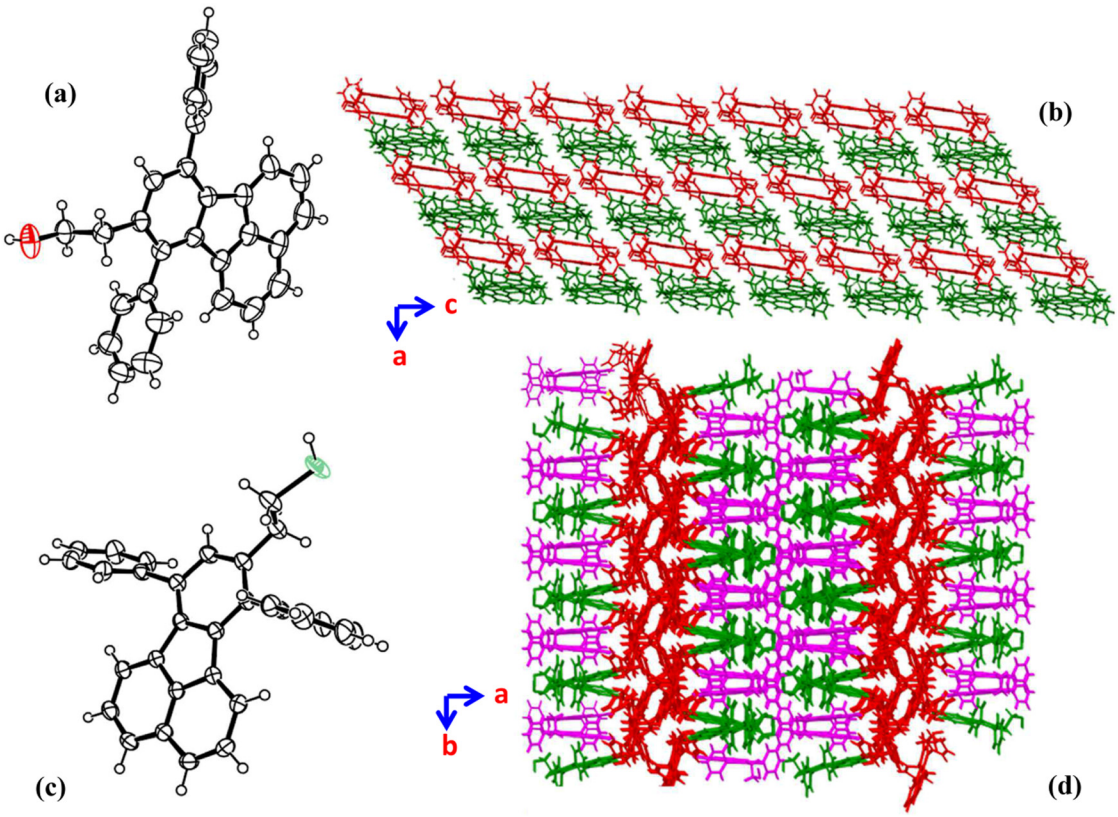

Fig. 1 Crystal structure (asymmetric units with 30% thermal ellipsoids) and its supramolecular packing arrangement in the crystal lattice of FOH (a and b) and FSH (c and d).

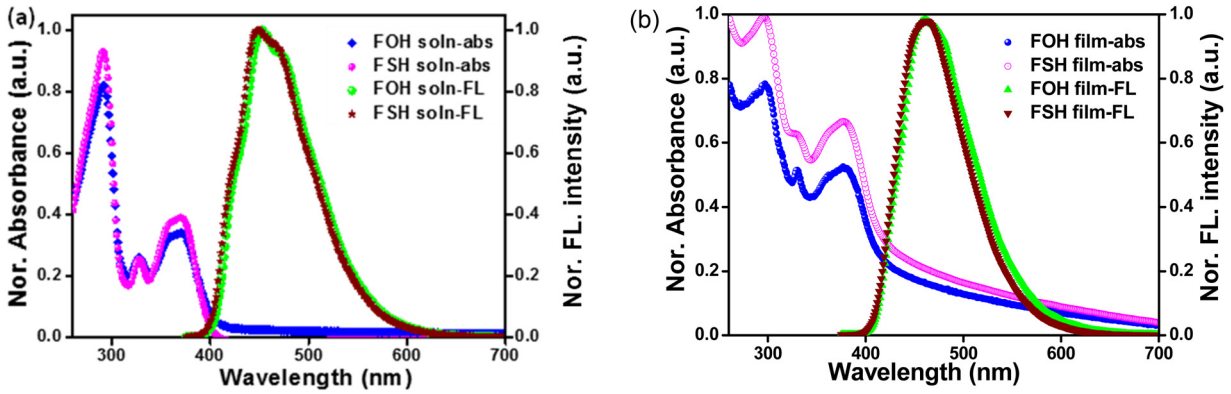

Fig. 2 Absorption (20 μM) and emission (1 μM) spectra of **FOH** and **FSH** in (a) THF solution and (b) thin film.

Table 1 Summary of the photophysical data of **FOH** and **FSH**

	Absorption λ_{abs} (nm)		Emission λ_{em} (nm)		Stoke's shift (nm)			Optical band gap (eV)	
Sample	Solution	Thin film	Solution	Thin film	Solution	Thin film	Lifetime (ns)	Solution	Thin film
FOH	291, 327, 371	296, 330, 377	453	461	82	84	24	3.02	2.86
FSH	291, 327, 371	296, 330, 378	447	463	76	85	15	3.04	2.82

functional effect, the relative emission intensity of **FSH** is observed to be higher. Table 1 outlines the photophysical characteristics of **FOH** and **FSH**. Fluorescence quantum yields (Φ) of **FOH** and **FSH** are observed to be ~30 and ~61%, respectively. The fluorescence lifetimes of **FOH** and **FSH** in THF exhibit a single exponential decay with lifetimes of ~26 and ~24 ns, while in thin films, they exhibit a dual lifetime with average lifetimes of ~10 and ~12 ns, respectively, using the time-correlated single photon counting (TCSPC) technique (Fig. S17a and b, ESI†). Table S2, ESI,† summarizes the photophysical data of the derivatives in solution and thin films. NACs interact strongly with surrounding excited fluorescent species despite having a severe electron deficiency. Fluoranthene derivatives are attractive for studying the detection of an incendiary nitro analyte by applying the fluorescence quenching method owing to their great stabilization and electron-rich surroundings. Both fluoranthene materials were investigated with various analytes, such as TNP, 2,4-dinitrophenol (DNP), 4-nitrophenol (NP), 3-nitrotoluene (3-NT), nitrobenzene (NB) and nitromethane (NM). Fluorescence titration studies of the fluoranthene derivatives (1 μM) were conducted upon the gradual inclusion of different NACs (1 mM) at varying concentrations, and the changes in the emission spectra were measured. It was found that the intensity of the fluorescence reduced gradually upon the progressive addition, owing to the electron transfer process that occurred amid the fluoranthene and nitro analytes.

Fig. 3a demonstrates the quenching efficiency of **FOH** and **FSH** fluorophores treated with various nitro analytes. Further, compared with other analytes, such as DNP, NP and NB, it is evident that both fluorophores show superior sensitivity towards TNP and exhibit ~78 ± 7% quenching efficiency. The feeble intermolecular interactions and efficient attraction

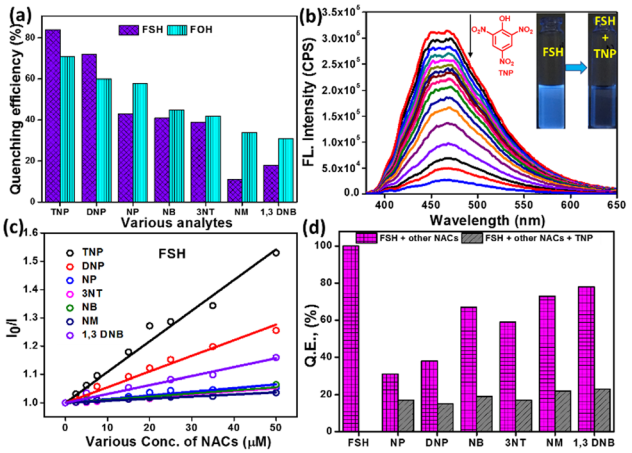

Fig. 3 (a) Variation in the quenching efficiency of 1 μM of **FOH** and **FSH** treated with various nitrated analytes (500 μM) in THF. (b) Changes in the emission intensity of **FSH** (1 μM) upon treatment with various concentrations of TNP (500 μM) in THF. (c) Stern–Volmer plot of **FSH** (1 μM) was treated with 50 μM of various nitro analytes. (d) Interference study of **FSH** (1 μM) with TNP (500 μM) in the presence of other analytes (500 μM).

with TNP *via* intercalation may be identified to make **FSH** significantly more sensitive than **FOH**.[25] The quenching efficiency of **FSH** is ~1.2 folds higher than that of **FOH** for TNP and DNP. The discrepancy in the quenching efficiency is mostly related to changes in the donor–acceptor interaction between the electron-deficient nature of the nitro analytes and the distinct functionality of fluoranthene.

The trend indicates that quenching efficiency maintains the sequence of TNP > DNP > NP > NB ~ 3NT > NM (Fig. S18a–f, ESI†). Fig. 3b shows the progressive reduction in the emission

intensity upon the incremental inclusion of TNP. The fluorescence response of **FSH** is entirely quenched. Further, the inset photograph shows visual turn-off fluorescence behaviour earlier and later inclusion of TNP to **FSH,** under UV light illumination at 365 nm. The fluorescence titration studies were accomplished to measure the sensing behaviour of 1 μM of **FOH** with various nitro analytes at different concentrations, as illustrated in Fig. S19a–g, ESI.† The reduction in emission intensity could represent an electron transfer mechanism based on static and dynamic quenching process. Fig. 3c shows the Stern–Volmer (K_{SV}) plot of **FSH** treated with various nitro analytes.

The K_{SV} values are determined according to our earlier report.[27] From the figure, it is clear that I_0/I values increase linearly as a function of concentration, indicating the predominance of the static quenching process. This suggests that the formation of a non-fluorescent ground state complex, which later returns to the ground state without emitting light, is responsible for the creation of static quenching. Summary of the K_{SV} values of **FSH** and **FOH** are tabulated in Table S3, ESI.† The K_{SV} values are invariant based on the type of nitro analytes and are found to be NM (7×10^2 M^{-1}), NB (1.1×10^3 M^{-1}), 3NT (1.4×10^3 M^{-1}), NP (1.3×10^3 M^{-1}), 1,3 DNB (3.1×10^3 M^{-1}), DNP (5.5×10^3 M^{-1}) and TNP (1.1×10^4 M^{-1}). Fig. S20, ESI† shows the Stern–Volmer rate constants of **FOH** with various nitro analytes and are found to be NM (7×10^2 M^{-1}), NB (1.3×10^3 M^{-1}), 3NT (1.3×10^3 M^{-1}), NP (1.7×10^3 M^{-1}), 1,3 DNB (3.5×10^3 M^{-1}), DNP (5.1×10^3 M^{-1}) and TNP (1.0×10^4 M^{-1}), respectively. Further, the LODs were determined by monitoring the fluorescence emission intensities of **FSH** with an increasing order of TNP concentrations, as illustrated in Fig. S21a, b and Table S4, ESI.† LOD = $3.3 \times \sigma/m$, where σ is the standard deviation and m is the slope, was used to calculate the LODs with ~97 ppm towards TNP. The reproducibility of the data was tested for three independent experiments to determine the error analysis. In most cases, the dispersion of error is found between ±292, and the data were represented with an average standard deviation. The selective detection of analytes plays an essential role in real-world applications. Moreover, interference fluorescence quenching studies were conducted to explore the selectivity of **FSH** for detecting TNP in THF in the presence of other nitroanalytes. In a typical experiment, initially, the **FSH** emission spectrum was noted. Further, effective access interactions with **FSH** and NB (50 μM) solution were added to this solution, and the emission spectra were recorded. With the addition of NB, we did not notice any appreciable changes in fluorescence quenching. An identical quantity of TNP was included in this solution, and the quenching of fluorescence efficiency changed drastically. A similar procedure was carried out with varying concentration cycles of NB and TNP. We observed that as the TNP concentration increased, fluorescence quenching decreased significantly. The experiment was repeated with the inclusion of TNP solutions for various NACs, and the variation in quenching efficiency is demonstrated in Fig. 3d. The gradual decrease in quenching efficiency specifies **FSH's** excellent selectivity to TNP in the presence of other interfering NACs in THF.

To gain more insight to understand the molecular interactions of fluorophores with NACs, partial ^{1}H-NMR titration studies were carried out between **FSH** and TNP (Fig. 4). The inclusion of TNP to **FSH** by the mole relation from 0.25 : 1 to 1 : 3 detected substantial variations in the TNP-aromatic protons. Upon the addition of a 0.25 mole ratio of TNP to **FSH**, the singlet signal at δ 9.06 ppm corresponding to the TNP started to appear, and the intensity of the signal progressively upsurges with an increase in the concentration of TNP, showing the slow conversion of the singlet proton into a double peak with a downfield chemical shift of δ 0.04 ppm. This mainly arises owing to the interaction between the **FSH** and TNP. Further, the α-protons of the naphthalene unit of fluoranthene at δ 7.67 ppm exhibit a significant interaction upon the addition of TNP. Initially, these protons resonated as multiplet and subsequently increased with the concentration of TNP (**FSH** : TNP, 1 : 1 mole ratio), and they were converted into a quartet towards the shielded regions, as demonstrated in Fig. 4. In the same manner, substituted phenyl protons and β proton of the naphthalene unit at δ 7.56 slightly shifted to the down-field upon the inclusion of TNP. With a further increase in the concentration of TNP, the signals further shifted towards the down-field. Concomitantly, the additional signals of phenyl ring protons showed feeble interactions. This is owing to the π–π intermolecular interactions between fluorophore and TNP, resulting in the adduct development of **FSH** with TNP.

It is interesting to note that during the synthesis of **FSH**, efforts were made to recrystallize the compound using different solvent systems. The reaction mixture is recrystallized in chloroform:methanol medium. The **FSH** crystallized and good quality single crystals were obtained. Suitable crystals were isolated, single-crystal X-ray data were collected, and the structure was elucidated.

Fig. 5a shows the crystal structure of the **FSH** adduct with 1,3-dinitro benzene (DNB). In the crystal lattice, **FSH** exhibits a ladder-type molecular packing arrangement, whereas the adduct form of **FSH** (**FSH**-adduct, CCDC: 2231960†) exhibits an M-type supramolecular framework (Fig. 5b). The structure reveals that DNB is stacked on the surface of the naphthalene ring and is mainly stabilized by π–π stacking distances of 3.473 and 3.449 Å with the $P2_1/c$ space group, and intermolecular

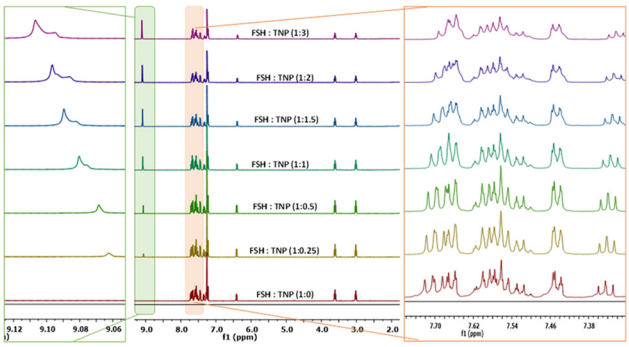

Fig. 4 Partial ^{1}H NMR (500 MHz) spectra of **FSH** upon the inclusion of different equivalents of TNP in $CDCl_3$.

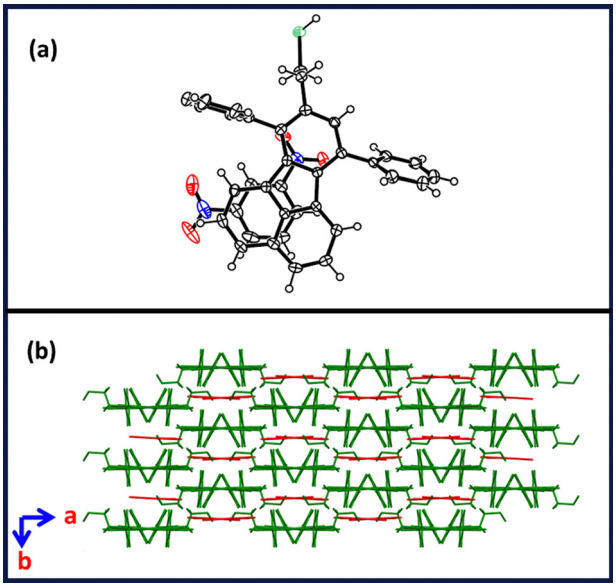

Fig. 5 Crystal structure of FSH.DNB adduct (asymmetric units with 30% thermal ellipsoids) and (b) its supramolecular packing arrangement in the crystal lattice.

hydrogen bonding is between N–H···O (2.626 Å), C–S···C (3.540 Å) and C–S···H (3.087 Å), C–S···O (4.286 Å). The aromatic C–H···H (2.263 Å), apart from the methylene group, forms hydrogen bonding interactions with aromatic C–H···H (2.912 Å) (Fig. S15c and Table S1, ESI†). Further, in the **FSH**·DNB adduct, the sulphur atom demonstrates the bonding interaction with another molecule phenyl component of the fluoranthene unit with a distance of 3.427 Å. Further, the **FSH**.DNB adduct displays the S–H four splitting interaction with the phenyl unit of another molecule, fluoranthene. The fluoranthene unit at the position of C(14) displays bonding interaction with DNB situated at C2 with a distance of 3.322 Å. The DNB displays two hydrogen bonding interactions at the positions of N(1)–O(3) and N(1)–O(4) with the phenyl moiety of fluoranthene located at C(25)–H(25) and C(34)–H(34) along with distances of 2.602 and 2.702 Å, respectively. Furthermore, the HRMS spectra of the **FSH**-adduct exhibited the molecular ion peak 581.2500 $[M - H]^+$, and the NMR (^1H, ^{13}C) investigation confirmed the desired molecular adduct. Based on the NMR and formation of molecular **FSH**.DNB adduct, a similar kind of molecular interaction occurs between **FSH** and TNP, resulting in an efficient molecular adduct formation furnishing its selective and sensitive detection.

To further understand the mechanism of fluorescence quenching, fluorescence lifetime titration experiments were carried out to ascertain the excited state interactions of fluoranthene with nitro analytes. The fluorescence lifetime of **FSH** at varying concentrations of TNP solution was demonstrated to be invariant (Fig. 6 and Table S5, ESI†), suggesting the presence of a ground state complex between **FSH** and TNP in a static manner. At very high concentrations of TNP, dynamic behaviour was observed.

The sensing process was investigated between probes and TNP by performing UV-Vis titration experiments, and its

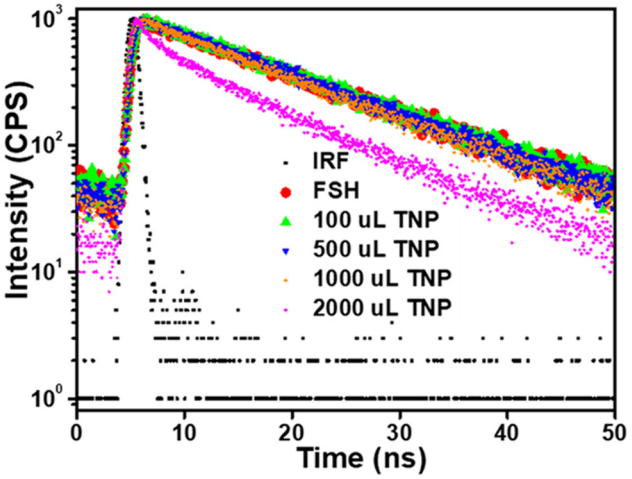

Fig. 6 Fluorescence lifetime decay of **FSH** (10 μM) with various concentrations of (50, 250, 500 and 1000 μM) TNP.

isotherms are shown in Fig. S22a–d (ESI†). In THF (Fig. S22a and c, ESI†), the probes **FSH** and **FOH** exhibit distinct characteristic absorption bands at 371 nm owing to the π → π* transitions. In addition to different concentrations of TNP (0–20 μM), the absorbance band at ~371 nm is gradually increased owing to the strong interaction between fluorophore and TNP. Fig. S22b and d (ESI†) show the UV-Vis isotherm of fluorophore (20 μM) upon the addition of TNP, [TNP]: 0–20 μM.

Furthermore, upon increasing the concentration of TNP, the absorbance band at 371 nm gradually increased in both fluorophores. Because each molecule exhibits identical absorption signatures and spectra fluctuations, it indicates that probable donor–acceptor complexes were formed amid π-electron rich fluoranthene ensembles and TNP. Similar absorption changes were observed with the addition of **FOH** to TNP. The lowest unoccupied molecular orbital (LUMO) levels of the NACs and the highest occupied molecular orbital (HOMO) levels of the luminogen showed critical roles in electron transfer-based fluorescence quenching. Consequently, the frontier molecular orbitals of the fluoranthene molecule were determined by calculation, and the results are illustrated in Fig. 7. Gaussian 09 software was used to optimise the geometry of **FSH**, **FOH** and TNP using the B3LYP/6-31g* basis sets.[40] HOMO orbitals of **FSH** have significantly delocalised on ethane thiol (of fluoranthene unit), while in **FOH**, it is localised on the fluoranthene. The LUMO orbitals appeared primarily on the fluorophore strand in both instances. Fluorescence fading includes the movement of electrons from the LUMO of the fluoranthene to the LUMO of the nitro analytes in their excited states.

Detection limits are determined by the effectiveness of this progression, which can be amended by enhancing NAC–fluoranthene binding interactions and combining the frontier molecular orbital energies of the fluoranthene with the LUMO of the nitrated analytes. As reported in the literature, analyte–fluorophore interactions in which nitrated compounds penetrate the cavities generated by substituting the phenyl group of fluoranthene and are anchored by intense intermolecular

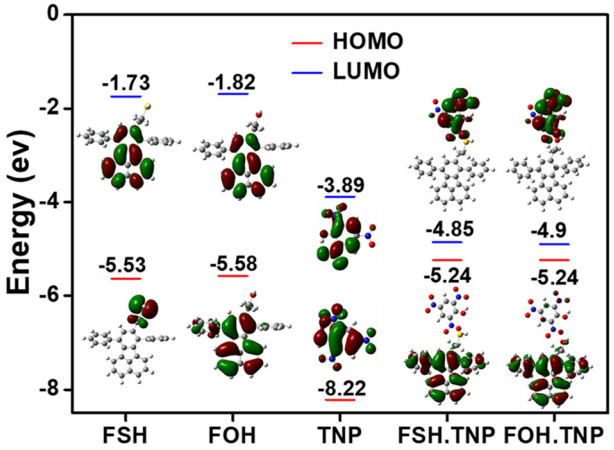

Fig. 7 HOMO and LUMO energy level diagrams of **FSH**, **FOH**, TNP and its adduct form of **FSH**·TNP, **FOH**·TNP obtained using B3LYP/6-31g* basis set in Gaussian 09.

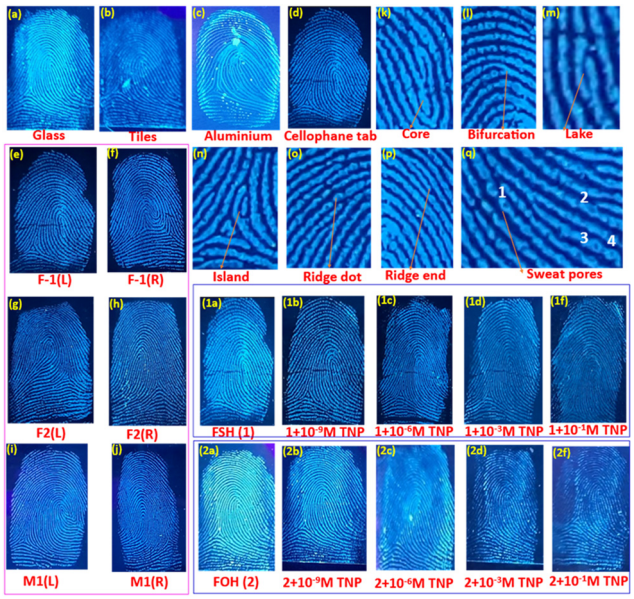

Fig. 8 LFPs of a right thumb created on various substrates, including glass, tiles, aluminium and cellophane tab, using **FSH** fluorophore (a)–(d). LFPs of the left and right thumbs of two females (e)–(h). LFPs of the left and right thumbs of one male (i) and (j). The latent fingerprint of the female left thumb is observed under long UV illumination (365 nm) to measure the type-2 particulars, such as (k) core, (l) bifurcation, (m) lake, (n) island, (o) ridge dot, (p) ridge ends and the type-3 details, (q) sweat pores. The image was established before and after the mixing of different concentrations of TNP with **FSH** (1a–f) and **FOH** (2a–f) molecules under the illumination of 365 nm light.

interactions and π–π interactions.[25] Further, in our previous report, alkyl chain substitution on the peripheral position of fluoranthene plays a vital role in analyte–fluorophore binding interaction.[27] From energy level distribution, we could determine that the optical energy band gaps differ slightly depending on the nature of different functional groups present on the fluoranthene unit, ranging from 3.80 (thiol) to 3.76 eV (alcohol). The optical band gap of **FOH** is lower than that of **FSH** because of variations in functional groups. Moreover, the LUMO energy of **FOH** and **FSH** is near that of TNP, which may be the driving factor for electron transfer from fluorophore to nitrated analytes.

To illustrate the real-time and field applicability of **FSH** and **FOH**, latent fingerprint fluorescence imaging was measured. Handprints are an essential type of physical documentation because fingerprints play a significant role in person identifiable information and thus are distinct and everlasting for everyone. The LFPs were generated (5 mg of **FSH** dissolved in 10 mL of acetonitrile) by pressing the left and right thumbs against four surfaces, including glass, tiles, aluminium and cellophane tape (Fig. 8a–d). The fluorescence images of the developed fingerprints after air-blowing on the solid of **FSH** appeared blue under UV illumination (365 nm) and demonstrated an extremely good distinction amid the fluorophore ridges and non-fluorescent furrows. To illustrate the versatility of the progress of LFPs, LFPs from three diverse persons (two females and one male) were studied. LFPs were recorded with three unique people (left and right thumb), two females (Fig. 8e–h) and one male (Fig. 8i and j) and were investigated to demonstrate the adaptability to produce LFPs. However, three individuals placed their left and right thumbs on the cellophane tape, allowing for the recording of the frequency of visually distinct fingerprints under prolonged UV irradiation at 365 nm. In general, three major variations in fingerprint identification were used to identify a person. As shown in Fig. 8k, the first-level characteristics of core information are utilised primarily for pattern identification. Further, the second-level features (minutia points such as ridge ending, island and bifurcation) are unique, stable and are extensively utilised to distinguish the fingerprint. The characteristics of type-2 identification were shown in Fig. 8k–p, and their photographs of the core (k), bifurcation (l), lake (m), island (n), ridge dot (o), and ridge end (p) indicate high-resolution photos. Furthermore, the type-3 features (sweat pores and ridge contours) are measured from the ridges that provide exact and consistent specifics for particular fingerprint detection. As shown in Fig. 8q, the sweat pore image of level 3 was magnified and demonstrated the identification of a person without any inconsistency, verifying real-time analysis. The above exemplifies the advantages of the current approach for the small organic molecule progress of LFPs.

In addition, the significance of the on-site rapid detection of explosives was afforded by the visual variation in fluorescence intensity. As shown in Fig. 8(1a–f) and (2a–f), **FSH** (1) and **FOH** (2) were examined to analyze different concentrations of TNP (ranging from 10^{-1} M to 10^{-9} M). 5 mg of the **FSH** and 10 mL of 0.1 M of TNP were mixed and touched, followed by pressing in a cellophane tape and capturing the photograph. A similar procedure was performed for various concentrations of TNP, ranging from 10^{-3} M to 10^{-9} M with **FSH**. The image demonstrated with the 10^{-6} M concentration of the TNP with **FSH** shows the brightness of the fingerprint diminished (Fig. 8(1c)). However, upon treatment with a 10^{-6} M concentration of TNP with **FOH**, the core part of the fingerprint completely

disappeared with inconsistency (Fig. 8(2c)). Fig. 8(1f) and (2f) displays the fluorescence response of **FSH** and **FOH** with the treatment of 0.1 M concentrations of TNP at 365 nm illumination.

Towards environmental drinking water pollution, the sensing response observed in drinking and river water trials spiked with TNP, and the variation in the emission behaviour was evaluated to determine the real-world application of **FSH**. The samples of drinkable water were taken from a single source point at SRMIST, and the samples of river water were taken from the banks of the Palar River in Chengalpattu, Tamil Nadu. We observed no substantial variations in emission spectra after introducing drinking water to **FSH**, demonstrating that intake water comprises no trace of TNP. Fig. S23a and b, ESI,† illustrates that the stock of TNP (0.1 mM) solution was created with river water and recorded emission spectra of **FSH** with the incremental additions of TNP. Upon the addition of 10 μM TNP, we observed ∼24% of fluorescence quenching efficiency. Further injection of 25 μM of TNP, resulted in a 54% quenching response of **FSH**. However, the detection limit of the real sample observed for **FSH** towards TNP is ∼76 ppm (Table S4, ESI†). Moreover, Table S6, ESI,† displays the successful analysis for the determination of TNP in real samples (river water) with 76–80% recovery. Further, towards real-time applicability, we carried out the fluorescence studies in H_2O : THF, as shown in Fig. S23c and d, ESI.† The change was observed as a function of increasing the concentration of TNP with **FSH** and **FOH**. Increasing the concentration of TNP systematically decreases the emission intensity at ∼455 nm. The **FSH** in the THF : H_2O (1 : 1 v/v) mixture (quenching efficiency = 95%) exhibits a higher response towards TNP detection than in the THF medium (quenching efficiency = 84%). Similarly, in the case of **FOH**, the detection of TNP is higher in the THF : H_2O (1 : 1 v/v) mixture (quenching efficiency = 95%) than in the THF environment (quenching efficiency = 71%). Therefore, both fluorophores demonstrated sensing behaviour towards the detection of TNP in THF and THF : H_2O mixtures to develop real-time applications. Furthermore, **FSH** and **FOH** were evaluated in relation to electron donating targets, such as toluene and xylene, as demonstrated in Fig. S24a–d, ESI.† It has been observed that **FSH** and **FOH** are more successful at detecting electron-withdrawing targets, such as TNP and DNP, than electron-donating analytes, such as toluene and xylene. However, in the presence of metal ions, such as Na^+, Fe^{3+}, Mn^{2+} and Zn^{2+}, our fluorophores are highly sensitive and selective for TNP detection (Fig. S25a and b, ESI†), making them an effective real-time sensor. The outcome of the research reveals that **FSH** exhibits good sensitivity to the identification of TNP, which renders this compound unique in practical analysis and onsite applications.

Further, our fluorophores were tested on the model organism zebrafish to determine its real-time applicability. The zebrafish was choosen owing to their rapid growth, tiny stature, transparency and accessibility of use in behavioral experiments. The present investigation focused on the ability of zebrafish natural fluorescence to detect aquatic nitro analytes. To assess the developmental toxicity of **FOH**, **FSH** and TNP zebrafish embryos were tested following OECD fish embryo toxicity guidelines for 96 hours.[44] A range of concentrations, such as 10, 20, 40, 60, 80, and 100 μg mL^{-1} was used to obtain the median lethal concentration. Subsequently, the hatching rate of zebrafish embryos was also assessed from 48 h onwards until 96 h. In a separate set of experiments, 72 hpf zebrafish larvae were used to assess the fluorescence emitted by **FSH**, **FOH** and their quenching by TNP (Fig. 9a–d and Fig. S26a–d, ESI†). The lowest tested concentration of 10 μg mL^{-1} was chosen to study fluorescence activity on live zebrafish larvae. The fluorescence images were captured using Nikon Eclipse Ti2, New York, USA, along with their respective control images and analyzed through Image J software. Acute behavioural toxicity of **FSH** and **FOH** on adult zebrafish with a concentration of 10 mg L^{-1} to assess the swimming response, as demonstrated in Fig. S27a–c and S28a–c, ESI.† In addition, research on 4 hpf zebrafish embryos by the **FOH** and **FSH** demonstrates that they are less harmful. The percent mortality at the maximum concentration of 100 μg mL^{-1} exhibits 20–30% compared to control groups. However, a concentration-dependent delay in hatching was observed compared to the controls during the experiment.

As shown in Fig. S26a and b, ESI,† we found that the fluorescence percentage increased by ∼13.78% compared to the DMSO control. After adding TNP to the 24 well plates containing the larvae already treated with **FOH**, the percentage reduction in fluorescence compared to the **FOH** control is found to be only 3.018% (Fig. S26c and d, ESI†). Moreover, in the case of Fig. 9a-b, the **FSH** percentage increase of fluorescence is 4.99% compared to DMSO-treated zebrafish larvae. After adding TNP to the 24 well plates containing the larvae treated with **FSH**, the percentage reduction in fluorescence compared to the **FSH** control is found to be only 3.014% (Fig. 9c and d, ESI†). Acute behavior of zebrafish exposed to **FOH** shows bottom dwelling, with no mirror biting, responding to sound and fearful like normal fish. However, in the case of **FSH**, mirror biting and bottom dwelling

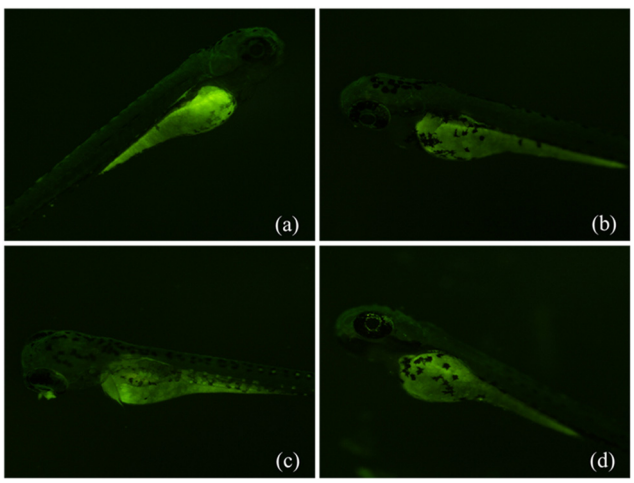

Fig. 9 **FSH** fluorescence quantification on 72 hpf zebrafish larvae: (a) water control, (b) DMSO and (c) **FSH** (d) **FSH** + TNP.

responses were observed. Zebrafish have natural green fluorescence throughout the body. However, easy visualization was observed in the yolk sac area. Zebrafish yolk sac acts as a nutrient reserve for the animal during its development and has dense amphiphilic environments with cholesterol, phosphatidylcholine, and phospholipo-glycoproteins.[45] Yolk sac can accumulate compounds from the surrounding environment using both active and passive modes;[46] therefore, it can act as a bio indicator. Further, we introduced fluorophores in the 24 well plates, which accumulated in the yolk sac area, and because these fluoranthenes also have fluorescence, the overall fluorescence increased in the zebrafish. A similar response was observed upon introducing TNP, which accumulated inside the yolk sac and caused an overall decrease in fluorescence. Most zebrafish exhibited aggressive behaviour after exposure to the fluorophore and TNP because they showed their response by mirror-biting. We observed an increase in the percentage of mirror-biting time in addition to extended periods spent near mirrors. Zebrafish may have mistaken their reflection for the real thing. However, this mirror stimulation had no impact on the zebrafish's locomotor activity. For the regular speediness, swim drive time ratio, freezing time movement ratio and no appreciable differences were found. Based on the results from acute behavioural toxicity testing for **FSH**, **FOH** along with TNP revealed that it is safe owing to the less neurological impact on the adult fishes within the tested concentration (Fig. S27a–c and S28a–c, ESI†).

4. Conclusions

In summary, we synthesized novel fluoranthene-based alcohol functionalized derivatives, and a facile approach for the conversion of aliphatic terminal alcohols to thiols was developed. The presence of different functional groups of the alkyl chain on fluoranthene rings generate distinctive supramolecular packing arrangements, including diagonal (**FOH**), ladder (**FSH**), and M-shape (**FSH**·DNB adduct), in the crystal lattice. The photophysical and theoretical investigations demonstrated that the optical gap was altered as a result of a change in functionality and an increase in the sensitivity of nitroanalytes. A solution phase fluorescence analysis demonstrates that **FSH** has higher quenching efficiency ($\sim$84%) and rate constant (K_{SV} = 1.1 $\times$ 10^4 M^{-1}), and a better detection limit (97 ppm in THF, 76 ppm in real sample) than **FOH**. In addition, the fluorescence lifetime measurements demonstrated that the static quenching mechanism distributes electrons from electron-rich fluoranthene to electron-deficient nitroanalytes. These fluorescent probes demonstrate a straightforward and profitable method for viewing LFPs with extremely consistent and realistic evidence of type 3 features without the requirement for LFPs to be post-treated. We expect that the current strategy will assist in the development of sensing material for TNP and other NACs, as well as be beneficial for the imaging of LFPs. Furthermore, the fluorophore is non-toxic and can be used as an effective model to study nitroanalyte contamination in zebrafish larvae.

Author contributions

Dr Venkatramaiah Nutalapati designed the research plan and execution, concept discussion, analysis of the results and contributed to the paper writing. Ms Kasthuri Selvaraj was involved in the synthesis, characterizations and fluorescence experiments related to chemosensing studies, data analysis and writing the manuscript. Mr. Prasanth Palanisamy was implicated in the synthesis, fluorescence experiments related to chemosensing studies and data analysis. Dr. Manikandan Marimuthu and Dr. Sangeetha Palanivelu provided support in PL data collection, ^{1}H and ^{13}C NMR data collection as well as reviewing the paper. Dr. Sohrab and Dr. Stepan Kment were involved in the analysis of photophysical properties. Dr. Sharmarke Mohamed and Dr. Praveen B. Managutti performed the single crystal X-ray diffraction data collection and structure solution. Dr. Rajesh Pamanji, and Prof. Joseph Selvin were involved in the toxicological studies of zebrafish, data analysis and review.

Conflicts of interest

The authors report no conflicts of interest.

Acknowledgements

S. Kasthuri acknowledges SRMIST and CSIR for Senior Research Fellowship (SRF). NVR thanks SERB for funding through the start-up research grant (SRG/2019/001023) and SRMIST for the seed grant. The authors also acknowledge the photoluminescence spectrometer facility, NRC and SCIF of SRMIST for analytical characterization. Rajesh Pamanji acknowledges the University Grant Commission (UGC), Govt. of India, for providing financial assistance in the form of Dr. DS Kothari Postdoctoral fellowship BL/19-20/0302. Furthermore, Operational Program Research, Development and Education – Projects No. CZ.02.1.01/0.0/0.0/15_003/0000416 and the funding from the Czech Science Foundation, project GA CR-EXPRO, 19-27454X. European Union under the REFRESH - Research Excellence For REgion Sustainability and High-tech Industries project number CZ.10.03.01/00/22_003/0000048 *via* the Operational Programme and ERDF/ESF project TECHSCALE (No.CZ.02.01.01/00/22_008/0004587).

References

1 (*a*) M. Chhatwal, R. Mittal, R. D. Gupta and S. K. Awasthi, Sensing ensembles for nitroaromatics, *J. Mater. Chem. C*, 2018, **6**, 12142; (*b*) V. Sathish, A. Ramdass, M. Velayudham, K.-L. Lu, P. Thanasekaran and S. Rajagopal, Development of Luminescent Sensors based on Transition Metal Complexes for the Detection of Nitroexplosives, *Dalton Trans.*, 2017, **46**, 16738–16769; (*c*) S. Shanmugaraju and P. S. Mukherjee, π-electron rich small molecule sensors for the recognition of nitroaromatics, *Chem. Commun.*, 2015, **51**, 16014–16032.

2 (*a*) G. S. Sodhi and J. Kaur, Powder method for detecting latent fingerprints: a review, *Forensic Sci. Int.*, 2001,

120, 172–176; (*b*) M. Wang, M. Li, A. Yu, Y. Zhu, M. Yang and C. Mao, Fluorescent Nanomaterials for the Development of Latent Fingerprints in Forensic Sciences, *Adv. Funct. Mater.*, 2017, **27**, 1606243; (*c*) C. Huynh and J. Halámek, Trends in Fingerprint Analysis, *Trends Anal. Chem.*, 2016, **82**, 328–336; (*d*) D.-H. Park, B. J. Park and J.-M. Kim, Hydrochronic Approaches to Mapping Human Sweat Pores, *Acc. Chem. Res.*, 2016, **49**, 1211–1222.

3 M. E. Germain and M. J. Knapp, Optical explosives detection: from color changes to fluorescence turn-on, *Chem. Soc. Rev.*, 2009, **38**, 2543–2555.

4 Y. Salinas, R. Martinez-Manez, M. D. Marcos, F. Sancenon, A. M. Costero, M. Parra and S. Gil, Optical chemosensors and reagents to detect explosives, *Chem. Soc. Rev.*, 2012, **41**, 1261–1296.

5 E. V. Verbitskiy, G. L. Rusinov, O. N. Chupakhin and V. N. Charushin, Design of fluorescent sensors based on azaheterocyclic push-pull systems towards nitroaromatic explosives and related compounds: A review, *Dyes Pigm.*, 2020, **180**, 108414.

6 T. F. Jenkins, D. C. Leggett and T. A. Ranney, *Vapor Signatures from Military Explosives Part 1. Vapor Transport from Buried Military-Grade TNT*, US Army Cold Regions Research and Engineering Laboratory, Special Report 99-21, Hanover, 1999.

7 US Environmental Protection Agency, Washington, DC, 2011.

8 A. R. W. Jackson and J. M. Jackson, *Forensic Science*, Prentice Hall, Harlow, England, 2nd edn, 2008.

9 J. Xu, B. Zhang, L. Jia, Y. Fan, R. Chen, T. Zhu and B. Zhong Liu, Dual-mode, Color-tunable, Lanthanide-Doped Core-Shell Nanoarchitectures for Anti-counterfeiting Inks and Latent Fingerprint Recognition, *ACS Appl. Mater. Interfaces*, 2019, **11**, 35294–35304.

10 R. E. Boseley, B. N. Dorakumbura, D. L. Howard, M. D. de Jonge, M. J. Tobin, J. Vongsvivut, T. T. M. Ho, W. V. Bronswijk, M. J. Hackett and S. W. Lewis, Development of luminescent sensors based on transition metal complexes for the detection of nitroexplosives, *Anal. Chem.*, 2019, **91**, 10622–10630.

11 F. Meng, J. Lian, W. Wang and Z. Zhang, Recent trends in fluorescent organic materials for latent fingerprint imaging, *Front. Chem.*, 2020, **8**, 594864.

12 R. G. Ewing, D. A. Atkinson, G. A. Eiceman and G. J. Ewing, A critical review of ion mobility spectrometry for the detection of explosives and explosive related compounds, *Talanta*, 2001, **54**, 515–529.

13 J. E. McFee, A. A. Faust, H. R. Andrews, E. T. H. Clifford and C. M. Mosquera, Nuclear instruments and methods in physics research section A: accelerators, spectrometers, detectors and associated equipment, *Nucl. Instrum. Methods Phys. Res.*, 2013, **712**, 93–101.

14 J. Yinon, Analysis and Detection of Explosives by Mass Spectrometry, *Aspects of Explosives Detection*, 2009, ch. 8, pp. 147–169.

15 D. Marder, N. Tzanani, H. Prihed and S. Gura, Trace detection of explosives with a unique large volume injection gas chromatography-mass spectrometry (LVI-GC-MS) method, *Anal. Methods*, 2018, **10**, 2712–2721.

16 (*a*) Z. Hu, B. J. Deibert and J. Li, Luminescent metal–organic frameworks for chemical sensing and explosive detection, *Chem. Soc. Rev.*, 2014, **43**, 5815–5840; (*b*) S. S. Nagarkar, A. V. Desai, P. Samanta and S. K. Ghosh, Aqueous phase selective 2,4,6-trinitrophenol detection via fluorescent metal-organic framework with pendant recognition site, *Dalton Trans.*, 2015, **44**, 15175–15180.

17 G. Das, B. P. Biswal, S. Kandambeth, V. Venkatesh, G. Kaur, M. Addicoat, T. Heine, S. Verma and R. Banerjee, Chemical Sensing in Two Dimensional Porous Covalent Organic Nanosheets, *Chem. Sci.*, 2015, **6**, 3931–3939.

18 J. Geng, P. Liu, B. Liu, G. Guan, Z. Zhang and M.-Y. Han, A Reversible Dual-Response Fluorescence Switch for the Detection of Multiple Analytes, *Chem. – Eur. J.*, 2010, **16**, 3720–3727.

19 K. Zhang, H. Zhou, Q. Mei, S. Wang, G. Guan, R. Liu, J. Zhang and Z. Zhang, Instant Visual Detection of Trinitrotoluene Particulates on Various Surfaces by Ratiometric Fluorescence of Dual-Emission Quantum Dots Hybrid, *J. Am. Chem. Soc.*, 2011, **133**, 8424–8427.

20 K. Kumar, H. Singh, V. Vanita, R. Singh, K. B. Joshi, G. Bhargava, S. Kumar and P. Singh, Coronene diimide-based self-assembled (fibre-to-disc) fluorescent aggregates for visualization of latent fingerprints, *Sens. Actuators, B*, 2019, **283**, 651–658.

21 P. Singh, H. Singh, R. Sharma, G. Bhargava and S. Kumar, Diphenylpyrimidinone-salicylideneamines - New ESIPT based AIEgens with applications in latent fingerprinting, *J. Mater. Chem. C*, 2016, **4**, 11180–11189.

22 G. Yun, J. J. Richardson, M. Capelli, Y. Hu, Q. A. Besford, A. C. G. Weiss, H. Lee, I. S. Choi, B. C. Gibson, P. Reineck and F. Caruso, The Biomolecular Corona in 2D and Reverse: Patterning Metal-Phenolic Networks on Proteins, Lipids, Nucleic Acids, Polysaccharides, and Fingerprints, *Adv. Funct. Mater.*, 2019, **30**, 1905805.

23 D. Li, J. Liu, R. T. K. Kwok, Z. Liang, B. Z. Tang and J. Yu, Supersensitive detection of explosives by recyclable AIE luminogen-functionalized mesoporous materials, *Chem. Commun.*, 2012, **48**, 7167–7169.

24 N. Venkatramaiah, S. Kumar and S. Patil, Fluoranthene based fluorescent chemosensors for detection of explosive nitroaromatics, *Chem. Commun.*, 2012, **48**, 5007–5009.

25 N. Venkatramaiah, S. Kumar and S. Patil, Femtogram detection of explosive nitroaromatics: fluoranthene-based fluorescent chemosensors, *Chem. – Eur. J.*, 2012, **18**, 14745–14751.

26 S. Kumar, N. Venkatramaiah and S. Patil, Fluoranthene based derivatives for detection of trace explosive nitroaromatics, *J. Phys. Chem. C*, 2013, **117**, 7236–7245.

27 S. Kasthuri, S. Kumar, S. Raviteja, B. Ramakrishna, S. Maji, N. Veeraiah and N. Venkatramaiah, Influence of alkyl chains on fluoranthene ensembles towards fluorescence-based detection of 2,4,6-trinitrophenol, *Appl. Surf. Sci.*, 2019, **481**, 1018–1027.

28 K. Selvaraj, P. B. Managutti, S. Mohamed, S. Talam and V. Nutalapati, Importance of the donor unit on fluoranthene for selective detection of nitro aromatic explosives, *J. Photochem. Photobiol., A*, 2022, **433**, 114215.

29 (*a*) N. Venkatramaiah, A. D. G. Firmino, F. A. A. Paz and J. P. C. Tomé, Fast detection of nitroaromatics using phosphonate pyrene motifs as dual chemosensors, *Chem. Commun.*, 2014, **50**, 9683; (*b*) J. Vastra and L.-S. Jalmes, Catalytic mesylation of alcohols: a highly productive process for trifluoroethyl mesylate, *Org. Process Res. Dev.*, 2006, **10**, 94–197.

30 H. Jia, Q. Li, A. Bayaguud, S. She, Y. Huang, K. Chen and Y. Wei, Tosylation of alcohols: an effective strategy for the functional group transformation of organic derivatives of polyoxometalates, *Sci. Rep.*, 2017, **7**, 1–9.

31 J. Pan, J. Xu, Y. Zhang, L. Wang, C. Qin, L. Zeng and Y. Zhan, A novel fluorescent probe for rapid and sensitive detection of hydrogen sulfide in living cell, *Spectrochim. Acta, Part A*, 2016, **168**, 132–138.

32 L. F. Fieser and M. Fieser, *Natural products related to phenanthrene*, Reinhold Publishing Corporation, New York, 1949, p. 892.

33 K. R. Bharucha, G. C. Buckley, C. K. Cross, L. J. Rubin and P. Zlegler, The conversion of hyodesoxycholic acid to progesterone, *Can. J. Chem.*, 1956, **34**, 982–990.

34 F. C. Chang, R. T. Blickenstaff, A. Feldstein, J. R. Gray, G. S. McCaleb and D. H. Sprunt, Seroflocculating steroids. II. 1 General2, *J. Am. Chem. Soc.*, 1957, **79**, 2161–2163.

35 F. C. Chang, A. Feldstein, J. R. Gray, G. S. McCaleb and D. H. Sprunt, Seroflocculating steroids. IV. 1 Unsaturated bile acid esters2, *J. Am. Chem. Soc.*, 1957, **79**, 2167–2170.

36 J. H. Lee, S. D. Yeo, D. Y. Jeong, S. H. Kim and J. H. Park, Products analysis in the reaction of substituted 1-phenylethyl alcohols with p-toluenesulfonyl chloride, *Bull. Korean Chem. Soc.*, 2000, **21**, 1005–1010.

37 P. A. Wiseman, S. Betras and B. Lindley, Conversion of a primary alcohol to an alkyl halide via a tosylate intermediate, *J. Chem. Educ.*, 1974, **51**, 348.

38 (*a*) V. B. Kurteva, B. L. Shivachev and R. P. Nikolova, Spontaneous conversion of O-tosylates of 2-(piperazin-1-yl) ethanols into chlorides during classical tosylation procedure, *R. Soc. Open Sci.*, 2019, **6**, 181840; (*b*) C. F. Allen and J. A. VanAllan, The synthesis of fluoranthene derivatives, *J. Org. Chem.*, 1952, **6**, 845–854.

39 S. Kasthuri, P. Gawas, S. Maji, N. Veeraiah and N. Venkatramaiah, Selective Detection of Trinitrophenol by Amphiphilic Dimethylaminopyridine-Appended Zn (II)phthalocyanines at the Near-Infrared Region, *ACS Omega*, 2019, **4**, 6218–6228.

40 M. J. Frisch, G. W. Trucks, H. B. Schlegel, G. E. Scuseria, M. A. Robb, J. R. Cheeseman, J. A. Montgomery Jr., T. Vreven, K. N. Kudin, J. C. Burant, J. M. Millam, S. S. Iyengar, J. Tomasi, V. Barone, B. Mennucci, M. Cossi, G. Scalmani, N. Rega, G. A. Petersson, H. Nakatsuji, M. Hada, M. Ehara, K. Toyota, R. Fukuda, J. Hasegawa, M. Ishida, T. Nakajima, Y. Honda, O. Kitao, H. Nakai, M. Klene, X. Li, J. E. Knox, H. P. Hratchian, J. B. Cross, V. Bakken, C. Adamo, J. Jaramillo, R. Gomperts, R. E. Stratmann, O. Yazyev, A. J. Austin, R. Cammi, C. Pomelli, J. W. Ochterski, P. Y. Ayala, K. Morokuma, G. A. Voth, P. Salvador, J. J. Dannenberg, V. G. Zakrzewski, S. Dapprich, A. D. Daniels, M. C. Strain, O. Farkas, D. K. Malick, A. D. Rabuck, K. Raghavachari, J. B. Foresman, J. V. Ortiz, Q. Cui, A. G. Baboul, S. Clifford, J. Cioslowski, B. B. Stefanov, G. Liu, A. Liashenko, P. Piskorz, I. Komaromi, R. L. Martin, D. J. Fox, T. Keith, M. A. Al-Laham, C. Y. Peng, A. Nanayakkara, M. Challacombe, P. M. W. Gill, B. Johnson, W. Chen, M. W. Wong, C. Gonzalez and J. A. Pople, *Gaussian 09, Revision A.02*, Gaussian, Inc., Wallingford CT, 2016.

41 J. von Euw and T. Reinchstein, *Helv. Chim. Acta*, 1946, **29**, 654–670.

42 R. T. Blickenstaff and F. C. Chang, Seroflocculating steroids. V. 1 Reduction of the bile acid side chain 2, 3, *J. Am. Chem. Soc.*, 1958, **80**, 2726–2730.

43 J. Ferns and A. Lapworth, *J. Chem. Soc.*, 1917, **01**, 273.

44 OECD, OECD TG 236 test guidelines for testing of chemicals, *Fish embryos acute toxicity (FET) tests*, 2013, pp. 1–22.

45 D. Fraher, A. Sanigorski, N. A. Mellett, P. J. Meikle, A. J. Sinclair and Y. Gibert, Zebrafish Embryonic Lipidomic Analysis Reveals that the Yolk Cell Is Metabolically Active in Processing Lipid, *Cell Rep.*, 2016, **14**, 1317–1329.

46 K. E. Sant and A. R. Timme-Laragy, Zebrafish as a Model for Toxicological Perturbation of Yolk and Nutrition in the Early Embryo, *Curr. Environ. Health Rep.*, 2018, **5**, 125–133.